MATERIALS SCIENCE

Reconfiguring band-edge states and charge distribution of organic semiconductor–incorporated 2D perovskites via pressure gating

Songhao Guo[1], Yahui Li[2], Yuhong Mao[1], Weijian Tao[3], Kejun Bu[1], Tonghuan Fu[1], Chang Zhao[3], Hui Luo[1], Qingyang Hu[1], Haiming Zhu[3], Enzheng Shi[2], Wenge Yang[1], Letian Dou[4]*, Xujie Lü[1]*

Two-dimensional (2D) semiconductor heterostructures are key building blocks for many electronic and optoelectronic devices. Reconfiguring the band-edge states and modulating their interplay with charge carriers at the interface in a continuous manner have long been sought yet are challenging. Here, using organic semiconductor–incorporated 2D halide perovskites as the model system, we realize the manipulation of band-edge states and charge distribution via mechanical—rather than chemical or thermal—regulation. Compression induces band-alignment switching and charge redistribution due to the different pressure responses of organic and inorganic building blocks, giving controllable emission properties of 2D perovskites. We propose and demonstrate a "pressure gating" strategy that enables the control of multiple emission states within a single material. We also reveal that band-alignment transition at the organic-inorganic interface is intrinsically not well resolved at room temperature owing to the thermally activated transfer and shuffling of band-edge carriers. This work provides important fundamental insights into the energetics and carrier dynamics of hybrid semiconductor heterostructures.

INTRODUCTION

Two-dimensional (2D) hybrid semiconductor heterostructures (HSHs) allow the properties to be designed at the molecular level by tailoring both the organic and inorganic components and by regulating their interfacial interactions (*1*–*6*). Manipulating the band-edge states and the consequent band alignments at the hybrid interfaces of HSHs yields key insights into the processes of photon-carrier conversion and charge distribution, which are central to modern technologies including (opto)electronics, data processing, and quantum devices (*7*–*10*). Carrier behavior at the interfaces of typical type I and type II aligned 2D heterostructures has revealed that the excited carriers would localize in a single component and separate at the interface, respectively (*11*–*13*). However, to the best of our knowledge, no research has elucidated the critical states between different band alignments and the corresponding carrier dynamics at the interfaces of HSHs. Besides, the reconfiguration process of the interfacial band states and its effects on optoelectronic properties remain unclear. Addressing these important questions requires suitable material systems in combination with advanced regulation and diagnostic tools that could enable the fine-tuning of electronic band structures and in situ characterization of the properties' evolution.

An appropriate hybrid heterostructure should have designable band-edge states and controllable interfacial interactions at atomic precision. Recently, 2D hybrid halide perovskites with conjugated organic cations have been developed, where the electronic states of the organic ligands extend to the band edges and could form different band alignments with the inorganic perovskite layers (*14*–*16*). The electronic and optical properties are therefore determined by both the organic and inorganic building blocks (ligand and perovskite, thereafter) and their interactions. These unique structures provide excellent opportunities for manipulating the band-edge states and charge distribution at the ligand-perovskite hybrid interfaces. The other challenge is the difficulty in continuously tuning the electronic band states while coupled with in situ property characterizations. Chemical methods including ion doping and molecular engineering have shown their capability in preparing hybrid heterostructures with designed interfaces (*17*–*19*), whereas a new sample needs to be synthesized for each band state, and the energy level cannot be continuously and precisely controlled (usually with the energy step over 0.1 eV) (*15*, *16*, *20*, *21*). As a thermodynamic parameter, pressure can effectively modify the lattice and electronic structures to realize diverse states in a single material (*22*–*28*). Thus, applying high pressure on these HSHs enables the tuning of their interfacial electronic structures and the band alignment in a controlled manner, where the building blocks of HSHs have different responses to pressure (*29*–*33*).

Here, by applying hydrostatic pressure to modulate the perovskite-ligand interactions, the band-edge states and charge distribution of various organic semiconductor–incorporated 2D halide perovskites are controllably manipulated toward designable optoelectronic properties. We have reached the critical states between different band alignments and achieved the desired band-alignment configurations that are previously unattainable. By using in situ high-pressure characterizations and first-principles calculations, we reveal the effects of band-alignment reconfiguration on their carrier dynamics and optoelectronic properties and unravel the underlying mechanisms of pressure gating. Our combined pressure and temperature regulation permits a clear picture for investigating the interfacial carrier dynamics. The charge distribution in frontier orbitals of organic ligands and perovskite layers is elucidated by a two-level thermal equilibrium model, which allows us to determine the energy level difference precisely by fitting the temperature-dependent photoluminescence (PL) spectra. This work offers new insights into the fundamental understanding of band-alignment engineering and provides innovative opportunities for the design of novel 2D hybrid heterostructures

[1]Center for High Pressure Science and Technology Advanced Research (HPSTAR), Shanghai, China. [2]School of Engineering, Westlake University, Hangzhou, China. [3]ZJU-Hangzhou Global Scientific and Technological Innovation Center, Hangzhou, China. [4]Davidson School of Chemical Engineering, Purdue University, West Lafayette, IN, USA.
*Corresponding author. Email: dou10@purdue.edu (L.D.); xujie.lu@hpstar.ac.cn (X.L.)

with diversified optoelectronic properties that can be achieved by manipulating the electronic edge states and their interactions.

RESULTS AND DISCUSSION

2D hybrid halide perovskites are built by alternatively arranged perovskite layers and organic ligands, where the electronic structures and, consequently, optical properties are determined by the interaction of these two components. To date, by extending the conjugation and reducing the electronic gap of organic ligands, three types of band alignment have been achieved, that is, type I with a band edge of conduction band minimum (CBM)–valence band maximum (VBM) from the perovskite layer, reverse type I with a band edge of lowest unoccupied molecular orbital (LUMO)–highest occupied molecular orbital (HOMO) from the organic ligand, and type II with a band edge of CBM-HOMO or LUMO-VBM (*16*). Figure 1 illustrates the three types of band alignment in three typical 2D halide perovskites as well as the corresponding structures and optoelectronic properties. The chemical structures of the four ligands mentioned in this study are exhibited in fig. S1, and the crystallographic information of the four 2D perovskites is listed in table S1.

In $(2T)_2PbI_4$ ($2T^+$ = bithiophenylethylammonium) with type I band alignment where the band-edge states are the CBM and VBM of $[PbI_6]^{4-}$ inorganic layers (Fig. 1A), excitons are strongly bounded in the perovskite layers, generating a strong and narrow excitonic emission with a peak at 525 nm and full width at half maximum of 16 nm. By reducing the bandgap of organic ligands, the electronic states of organic ligands can directly contribute to the frontier orbitals of 2D perovskites. $(4Tm)_2PbI_4$ ($4Tm^+$ = quaterthiophenylethylammonium) has type II band alignment (Fig. 1B), where the band-edge states are the CBM of $[PbI_6]^{4-}$ inorganic layers and the HOMO of the organic ligands. In such a configuration, the excitonic emission is quenched, suggesting efficient charge separation at the perovskite/ligand interface. As the bandgap of organic ligands further reduces, a reverse type I band alignment can be realized, where the band-edge states are dominated by the HOMO and LUMO of organic ligands (Fig. 1C). The 2D halide perovskite $(BTm)_2PbI_4$ [BTm^+ = 2-(4′-methyl-5′-(7-(3-methylthiophen-2-yl)benzo[c][1,2,5]thiadiazol-4-yl)-[2,2′-bithiophen]-5-yl)ethan-1-aminium] with reverse type I band alignment exhibits a red emission at ~660 nm from the BTm^+ ligands, whereas no PL from the inorganic layer is detected. Note that although the electronic states of $[PbI_6]^{4-}$ inorganic layers are similar for these three 2D perovskites, they exhibit remarkably different emission properties due to varied band-edge states and the different band alignments.

Here, we leave another question: What will happen when the energy levels of organic ligands and perovskite layers are very close? To address this important question, we introduce a conjugated $3T^+$ ligand [$3T^+$ = 2-([2,2′:5′,2″-terthiophen]-5-yl)ethan-1-aminium] to form a 2D perovskite $(3T)_2PbI_4$ (Fig. 2A) with an appropriate band structure. The energy levels of HOMO and VBM of $(3T)_2PbI_4$ are close (Fig. 2B), which makes the determination of the exact band alignment difficult by using ultraviolet (UV) photoelectron spectroscopy or cyclic voltammetry. We noticed that $(3T)_2PbI_4$ shows a similar but much weaker excitonic emission in comparison with

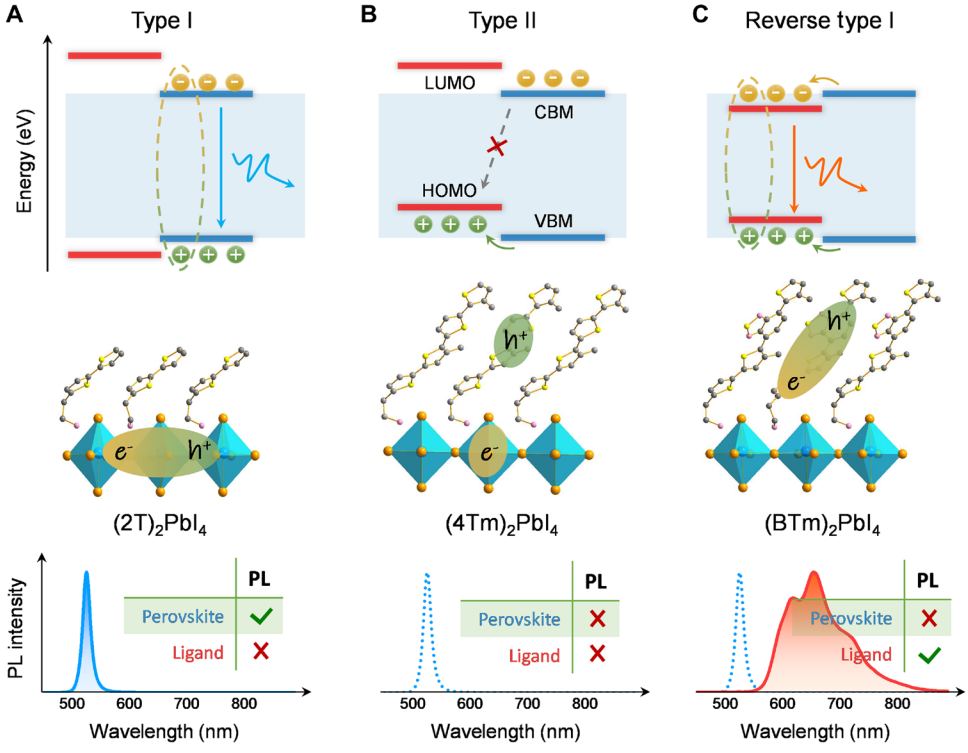

Fig. 1. The structure and excitonic behavior in various 2D hybrid halide perovskites. (**A** to **C**) Three types of band alignment of type I (CBM-VBM edged), type II, and reverse type I (LUMO-HOMO edged) are shown. Top: The energy level alignments of organic (red lines) and inorganic (blue lines) subunits, the exciton formation, charge separation, and emission processes. Middle: The crystal structures and the charge distributions. Bottom: The corresponding PL spectra of the 2D perovskites with different conjugated organic ligands (A) $(2T)_2PbI_4$, (B) $(4Tm)_2PbI_4$, and (C) $(BTm)_2PbI_4$. The blue and red PL spectra in the bottom are ascribed to the excitonic emission from perovskite layers and organic ligands, respectively, where the PL spectrum of $(2T)_2PbI_4$ is shown in blue dashed lines in (B) and (C) for reference.

$(2T)_2PbI_4$ with type I alignment (Fig. 2C). Intriguingly, the PL intensity of $(3T)_2PbI_4$ increases considerably upon cooling, which is different from the behavior of $(2T)_2PbI_4$ (fig. S2). To describe the charge distribution at HOMO and VBM of $(3T)_2PbI_4$, we introduce a two-level thermal equilibrium model, which follows the Boltzmann distribution

$$N_{HOMO} = N_{VBM} \times e^{-\frac{\Delta E}{kT}} \quad (1)$$

where N is charge density, k is the Boltzmann constant, and ΔE represents the energy level difference (i.e., $E_{VBM} - E_{HOMO}$). As is well known, the excitonic emission intensity is proportional to the charge density when the charge density is relatively low. According to this, we fit the temperature-dependent PL intensity of $(3T)_2PbI_4$ according to an Arrhenius equation

$$I(T) = \frac{I_0}{1 + Ae^{\left(-\frac{\Delta E}{kT}\right)}} \quad (2)$$

where I_0 is the integrated PL intensity extrapolated at 0 K, and A is a constant. As shown in Fig. 2D, the energy level difference ΔE between VBM and HOMO in $(3T)_2PbI_4$ is determined to be 52 meV, indicating its type I nature of band alignment. Note that the ΔE value is comparable to the room temperature thermal energy (26 meV), which allows the photoexcited carriers to be thermally activated and separated at the perovskite/ligand interface, thus resulting in the weak excitonic emission at room temperature. The excitons can be stabilized at the band-edge states of inorganic perovskite layers at lower temperatures that bring enhanced excitonic emission.

Thanks to the different pressure responses of the building blocks in the 2D halide perovskites, the interaction between perovskite layers and organic ligands can be regulated. We subsequently applied hydrostatic pressure to manipulate the band-edge states of $(3T)_2PbI_4$ toward controlled optoelectronic properties (Fig. 2E and fig. S3), where a sharp increase in PL intensity by ~15 times can be observed during compression. Such an enhanced PL intensity of $(3T)_2PbI_4$ at 2.1 GPa is comparable to that of typical type I aligned $(2T)_2PbI_4$ at ambient pressure, confirming the modulated electronic structure. To further reveal the energy level evolution of $(3T)_2PbI_4$ under high pressures, in situ low-temperature PL measurements are conducted (fig. S4). As exhibited in Fig. 2F, the fitted energy level difference ΔE gradually increases from 52 meV under ambient conditions to 167 meV at 1.8 GPa, which impels more photogenerated carriers to stay in the perovskite layers (VBM states), thus giving rise to the enhanced excitonic emission upon compression. Note that the underlying mechanism for the enhanced PL of $(3T)_2PbI_4$, that is, pressure-regulated band-edge states and charge carrier redistribution, is distinguished from the previously reported ones. Previous studies have demonstrated the pressure effects on PL enhancement of 2D perovskites by suppressing exciton trapping, optimizing exciton-phonon coupling, and regulating off-centering distortion (*25*, *32*–*35*).

Using the thermal equilibrium model and pressure regulation, the band-edge states of $(3T)_2PbI_4$ have been determined and continuously manipulated. In the following section, we will demonstrate that electronic structure engineering by pressure not only could manipulate the band-edge states and charge distribution of 2D halide perovskites but also is capable to induce band-alignment reconfiguration. For instance, we performed in situ high-pressure PL measurements at different temperatures for $(4Tm)_2PbI_4$ to explore the electronic structure evolution of 2D perovskites with initial type II band alignment (Fig. 3). With such an electronic configuration, no emission can be

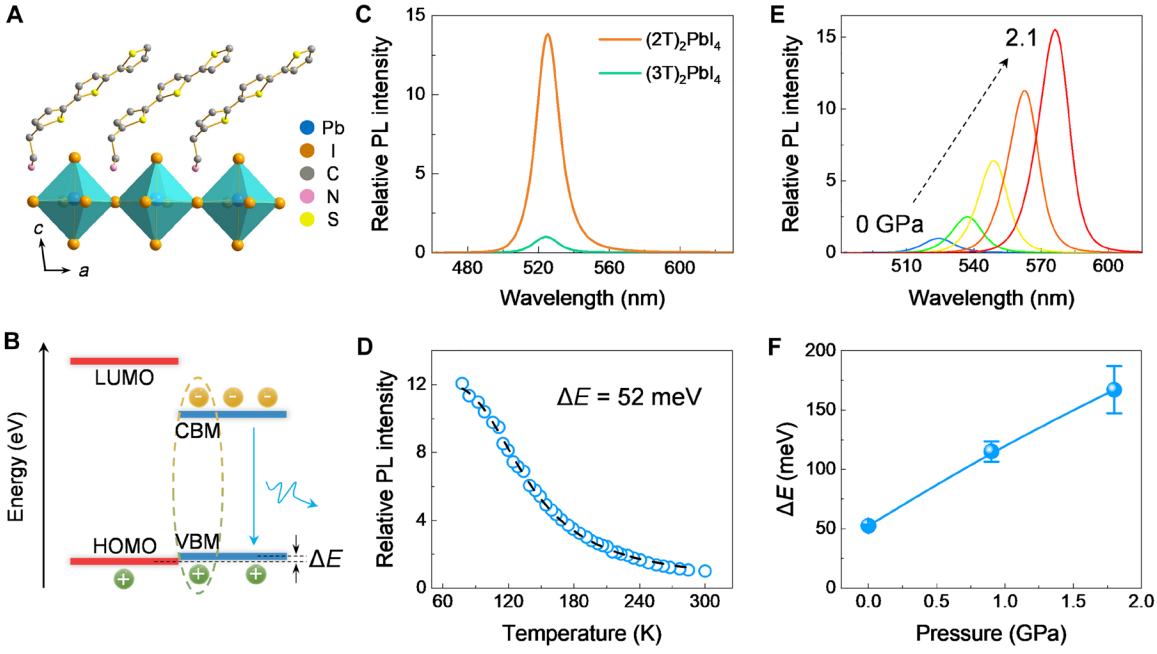

Fig. 2. Pressure-regulated band-edge states and charge distribution in 2D perovskite $(3T)_2PbI_4$. (**A**) The crystal structure. (**B**) Band alignment of organic ligands (red lines) and perovskite layers (blue lines). ΔE represents the energy level difference between VBM and HOMO. (**C**) PL spectra of $(3T)_2PbI_4$ compared with typical type I $(2T)_2PbI_4$ under ambient conditions. (**D**) The PL intensity as a function of temperature at ambient pressure. (**E**) In situ PL spectra upon compression. (**F**) The energy level difference ΔE as a function of pressure.

detected in $(4Tm)_2PbI_4$ at ambient pressure due to the efficient charge transfer from VBM to HOMO at the perovskite/ligand interface (Fig. 1B).

With pressure increasing, an excitonic emission peak emerged at ~3.7 GPa, as shown in Fig. 3A (color plot) and in fig. S5 (line plot). Such an emergent excitonic emission indicates the suppression of charge separation at the perovskite/ligand interface and the formation of stable excitons in the perovskite layers. Compression effectively manipulates the energy levels of both organic ligands and perovskite layers, and the different pressure responses of organic and inorganic parts would give rise to the band-alignment reconfiguration from type II at ambient pressure to type I at pressures beyond 3.7 GPa. Figure 3B shows the PL intensity of $(4Tm)_2PbI_4$ at 78 K as a function of pressure, which markedly increases at around 4 GPa and remains constant hereafter. As discussed above, thermal activation allows the photoexcited charges to occupy the high-energy levels, which could be more obvious at higher temperatures. We subsequently recorded the high-pressure PL spectra of $(4Tm)_2PbI_4$ at 300 K, shown as the color plot in Fig. 3C and line plot in fig. S6. The excitonic emission emerges at a lower pressure of 2 GPa at 300 K where the sample is still in type II band alignment, and no emission can be detected at 78 K. Figure 3D exhibits the PL intensity of $(4Tm)_2PbI_4$ at 300 K as a function of pressure, which gradually increases from 2 to 6 GPa. As illustrated in fig. S7, the type II band alignment of 2D halide perovskite switches to type I upon compression, which induces the excitonic emission; then, the energy difference ΔE between HOMO and VBM gradually enlarges with further pressurization, which allows more excitons to be stabilized in the perovskite layers, resulting in the exponentially enhanced emission. Note that the transition from type II to type I band alignment at room temperature is much worse resolved as compared with that at 78 K. This is again because the kinetic energy of charge carriers at room temperature is high enough to allow holes transferring and shuffling between two band-edge states across the organic-inorganic interface of hybrid heterostructures.

We further carried out femtosecond transient absorption (TA) spectroscopy to characterize the charge transfer and recombination processes at the organic-inorganic interface of $(4Tm)_2PbI_4$. As shown in Fig. 4A and fig. S8, the positive and negative features near the exciton transition energy can be assigned to the bleach of excitonic absorption and photon-induced absorption, respectively. The dynamics are fitted with a biexponential decay function, with a lifetime of ~9 and ~53 ps, while derivative spectral features emerge after 100 ps with a lifetime longer than 1 ns (limited by the time window of the measurements). Such long-lived spectral features come from the formation of a charge separation state at the ligand-perovskite hybrid interface. Upon compression, the long-lived spectral features gradually weaken, as shown in Fig. 4B and fig. S8, indicating the suppression of charge separation. We calculated the ratio of bleach peak maxima of the charge-separated state to the exciton state, which gradually decreases from 0.092 at 0.2 GPa to 0.034 at 5.3 GPa

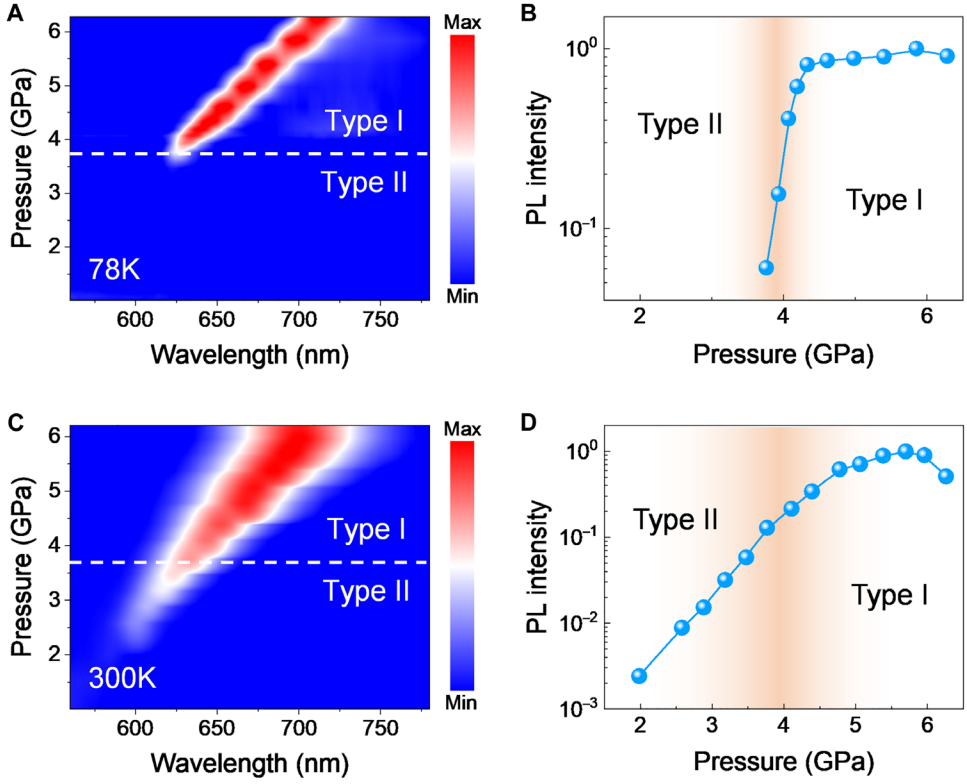

Fig. 3. Band-alignment reconfiguration and emission property evolution in 2D perovskite $(4Tm)_2PbI_4$ under high pressure. Pressure-dependent PL spectra at (**A**) 78 K and (**C**) 300 K. The PL intensity as a function of pressure at (**B**) 78 K and (**D**) 300 K. The band-alignment transition is intrinsically not well resolved at 300 K owing to the thermally activated transfer and shuffling of band-edge carriers, while the transition can be better defined at lower temperature.

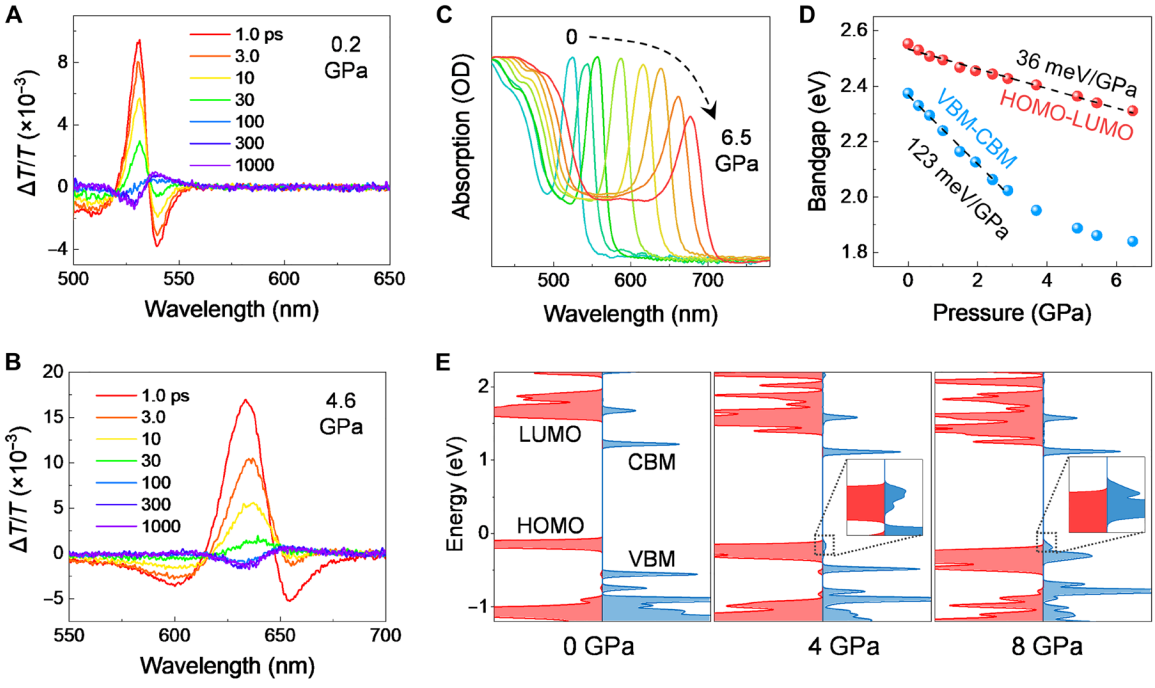

Fig. 4. Carrier dynamics and the manipulated band-edge states in 2D perovskite $(4Tm)_2PbI_4$. TA spectra at (**A**) 0.2 GPa and (**B**) 4.6 GPa, where the charge separation state gradually weakens during compression due to the reconfiguration of band states. (**C**) Absorption spectra at different pressures. OD, optical density. (**D**) Electronic gap of the perovskite layers (VBM-CBM) and organic ligands (HOMO-LUMO) as a function of pressure. (**E**) Calculated partial density of state for the perovskite layers (blue) and organic ligands (red) at different pressures.

(fig. S9). The suppression of charge separation further confirms the pressure-induced stabilization of excitons in the perovskite layers due to the band-alignment switching from type II to type I (Fig. 3).

To quantitatively determine the variations of electronic gaps of organic ligands and perovskite layers in $(4Tm)_2PbI_4$, in situ static UV-Vis absorption spectroscopies were performed at high pressures (Fig. 4C). Under ambient conditions, an excitonic absorption peak at 525 nm and a continuum absorption band below 490 nm are observed in $(4Tm)_2PbI_4$, which correspond to the transitions in perovskite layers and organic ligands, respectively. Intriguingly, the red shift of excitonic peak upon compression is much faster than that of the continuum absorption band. As shown in Fig. 4D, the value of pressure-induced bandgap variation for CBM-VBM of perovskite layers is fitted to be 123 meV/GPa, which is ~3.5 times larger than the electronic gap variation value for HOMO-LUMO of the organic ligands (36 meV/GPa), suggesting a less compressible nature of the conjugated organic ligands. Such a considerable difference in the compressibility for perovskite layers and organic ligands enables the reconfiguration of the frontier electronic states and thus triggers the band-alignment switching from type II at ambient pressures to type I at high pressures.

First-principles calculations for the electronic structures of $(4Tm)_2PbI_4$ at different pressures further verify the variations of band alignment (Fig. 4E and fig. S10). From the partial density of state of $(4Tm)_2PbI_4$ under ambient conditions, an obvious type II band alignment between the organic ligands and perovskite layers is observed, in line with the recently reported theoretical results (*36*). Upon compression, the electronic bandgap of perovskite layers (VBM-CBM) decreases more rapidly than that of the organic ligands (HOMO-LUMO), as shown in fig. S11, which is consistent with the bandgap evolution derived from in situ absorption measurements (Fig. 4D). Focusing on the movement of electronic bands, the valence band of the perovskite layers moves upward faster than that of the conjugated organic ligands with increasing pressure, resulting in the position swap of VBM and HOMO at the band edge (Fig. 4E). This behavior gives rise to the reconfiguration of the band alignment in the 2D hybrid halide perovskite, which agrees well with the experimental results.

In the case of $(4Tm)_2PbI_4$ with initial type II band alignment (Fig. 1B), the emission state from off to on has been controlled by reconfiguring the band alignment to type I (Fig. 1A). Another outstanding question arises, whether it is possible to realize the control of multiple emission properties (off state and various on states) within one sample by manipulating the band-edge states. To address this question, we further performed in situ PL measurement at 78 K for $(BTm)_2PbI_4$, which has initial reverse type I band alignment with the band edge of LUMO-HOMO from the organic ligand (Fig. 1C). As shown in Fig. 5A and fig. S12, the broad emission from BTm^+ ligands gradually vanishes during compression up to 2 GPa. This is caused by the pressure-induced reconfiguration of band alignment from reverse type I to type II (left and middle in Fig. 5B), since the electronic states of perovskite layers move faster than those of the conjugated organic ligands, as have been demonstrated in the $(4Tm)_2PbI_4$ sample (Fig. 4). Subsequently, a narrow excitonic emission peak emerged at around 3.5 GPa, owing to the further reconfiguration of the band alignment from type II to type I (middle and right in Fig. 5B). As shown in Fig. 5C, the in situ absorption spectra of $(BTm)_2PbI_4$ under high pressures reveal the electronic gap variations of BTm^+ organic ligand and $[PbI_6]^{4-}$ perovskite layers. Under ambient conditions, a strong excitonic absorption peak at 520 nm was observed, which corresponds to the perovskite layers, while a

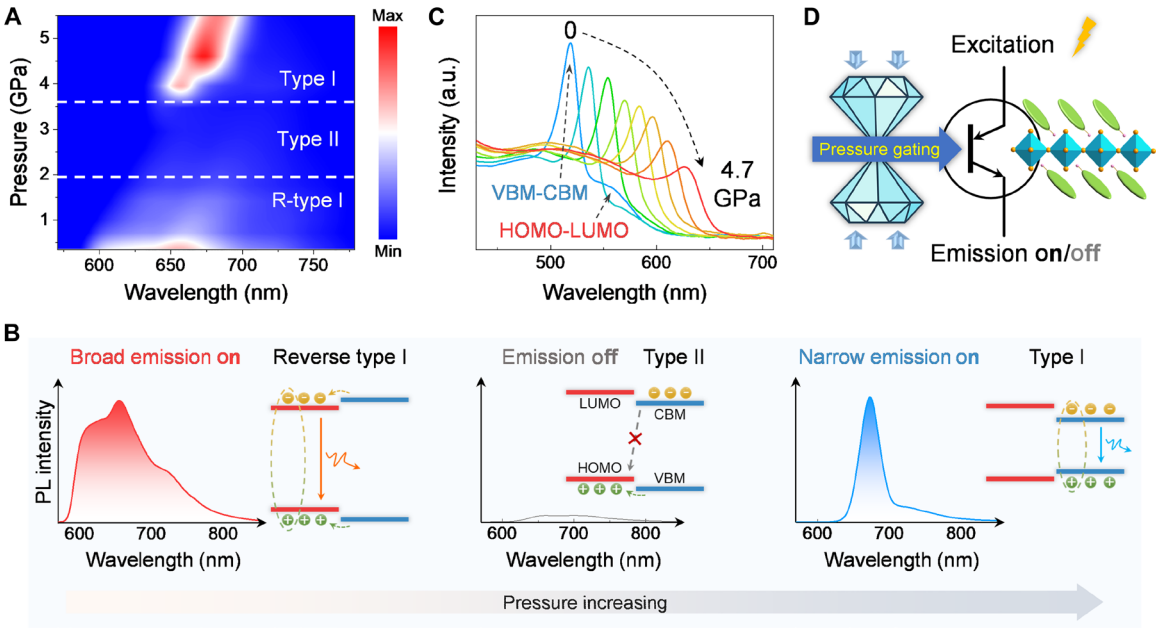

Fig. 5. Pressure-controlled multiple emission states of 2D perovskite $(BTm)_2PbI_4$. (**A**) In situ PL spectra at 78 K during compression. (**B**) Emission properties and the corresponding band alignments at different states with pressure increasing. (**C**) Absorption spectra at different pressures. a.u., arbitrary units. (**D**) Schematic illustration of pressure-gated multiple emission states where the emission on (both narrow and broad) or emission off can be controlled.

continuum absorption band at the low-energy side of the excitonic peak is from the BTm^+ ligand absorption. During compression, the excitonic absorption peak red shifts considerably, which moves faster than the BTm^+ ligand absorption band and eventually transcends the latter, confirming the pressure-induced reconfiguration of the band alignment.

The frontier electronic structures and optoelectronic properties of 2D halide perovskites with conjugated organic cations are determined by both the organic and inorganic building blocks and their interactions. Manipulating these interactions enables the designed band-edge states, band alignments, and, consequently, the controllable optoelectronic properties of these 2D perovskites. The additional degree of freedom for property tuning has attracted great interest that promotes the discovery of desired functionalities by using various tuning strategies such as electrical gating, magnetic field, and thermal heating. In this case, by reconfiguring the band alignment of $(BTm)_2PbI_4$, we have demonstrated that pressure could serve as a gate to control the emission with one off state and two on states (narrow and broad emission) (Fig. 5, B and D). Such a pressure gating strategy will inspire future materials design and may lead to potential applications including modulators, optical switches, and photonic chips. For materials design criteria, the switching threshold pressure can be tuned by adjusting the VBM-HOMO and CBM-LUMO energy offset; the pressure sensitivity can be tuned by adjusting the inorganic crystal lattice rigidity and tuning the molecular structures of organic ligands; the color tunability can be achieved by mixing halides (Cl—Br—I alloying), varying the quantum well thickness (*n* number of the inorganic layer), and changing the B-site metal elements. These design criteria can be applied to other materials beyond 2D perovskites that have different pressure responses of their building blocks.

In summary, by continuously regulating the energy levels of the organic and inorganic building blocks of organic semiconductor–incorporated 2D halide perovskites using external pressure, we have demonstrated the possibility to fine-tune the band-edge states and the charge distribution of the 2D semiconductor heterostructures previously unattainable. We subsequently achieved the critical states between different band alignments and elucidated the related carrier behaviors at the interfaces of HSHs. We have successfully reconfigured the band alignments in various 2D halide perovskites with different initial states, leading to redistributed band-edge carriers and thus the controllable optoelectronic properties. We have also revealed that the band alignments in these hybrid heterostructures are not well circumscribed owing to the thermal activation of band-edge carriers. The charge distribution in the perovskite layers and organic ligands can be described by a two-level thermal equilibrium model, and the energy level difference can thus be accurately determined by fitting the in situ temperature-dependent PL spectra.

In the meantime, different band alignments and diverse interlayer interactions have been widely studied in 2D van der Waals (vdW) materials, including vertical heterostructures of 2D halide perovskites and transition metal dichalcogenides, that have exhibited attractive optical and optoelectronic properties (*37*–*42*). The effective tuning of the interlayer coupling in WSe_2-$MoSe_2$ heterostructures has reported that a pressure-induced band changeover of interlayer excitons was observed (*43*). Different behaviors of interlayer energy or carrier transfer have been achieved by fabricating different vertical heterostructures of 2D perovskites via chemical methods (*40*–*42*). For these 2D halide perovskites and vdW semiconductors exhibiting different pressure responses of the building units, pressure processing not only provides an effective and clean manner to modulate their lattices but also offers new opportunities for achieving configurable electronic properties with designable band-edge states and band alignments. We believe that the principles presented in our work could serve as a blueprint for the design, production, and fine-tuning of

many other functional semiconductor heterostructures toward the realization of high performance by manipulating the band-edge states and the interfacial charge distribution.

MATERIALS AND METHODS

Sample preparation

The crystals of $(2T)_2PbI_4$, $(3T)_2PbI_4$, and $(4Tm)_2PbI_4$ were synthesized by a slow cooling method. For the $(2T)_2PbI_4$ single crystal: 0.03 mmol 2T·HI (hydroiodic acid) (98%; Feiming Technology Co. Ltd) and 0.01 mmol lead iodide (PbI_2; 99.999%; Xi'an Polymer Light Technology Corp.) were dissolved in 0.1 ml of HI (J&K Scientific), 0.05 ml of hypophosphorous acid (H_3PO_2; J&K Scientific), and 2 ml of isopropyl alcohol (IPA, Sinopharm). After heating to 100°C, the solution became clear. It was then cooled slowly to room temperature for 12 hours. For the $(3T)_2PbI_4$ single crystal: 0.01 mmol 3T·HI (98%; Feiming Technology Co. Ltd) and 0.02 mmol PbI_2 were dissolved in 0.1 ml of HI, 0.05 ml of H_3PO_2, and 2 ml of IPA. After heating to 100°C, the solution became clear. It was then cooled slowly to room temperature for 12 hours. For the $(4Tm)_2PbI_4$ single crystal: 0.02 mmol 4Tm·HI (98%; Feiming Technology Co. Ltd) and 0.01 mmol PbI_2 were dissolved in 0.1 ml of HI, 0.05 ml of H_3PO_2, and 2 ml of IPA. After heating to 100°C, the solution became clear. It was then cooled slowly to room temperature for 12 hours. Differently, the $(BTm)_2PbI_4$ bulk single crystal was synthesized via the antisolvent diffusion method. BTm·HI (0.04 mmol; 98%; Feiming Technology Co. Ltd) and 0.02 mmol PbI_2 were dissolved in 1 ml of γ-butyrolactone (Macklin Inc.). By adopting chlorobenzene (Sigma-Aldrich) and chloroform (Sinopharm; the volume ratio between chlorobenzene and chloroform is 1:1) as antisolvents, the $(BTm)_2PbI_4$ nucleated and grew up gradually into bulk crystals after 72 hours. After the crystal synthesis, the final crystals were collected by vacuum filtration, and the residue solvent was further removed in a vacuum chamber.

In situ high-pressure measurements

The high-pressure environment was provided by symmetrical diamond anvil cells. Type II-a ultralow-fluorescence diamonds with a culet size of 500 μm were used. The high-pressure sample chamber was formed from a preindented T301 gasket with a thickness of about 50 μm and a hole with a diameter of about 300 μm by laser drilling the center part of it. The as-prepared single crystals were exfoliated into thin flakes and transferred onto the diamond culets. The optical images of $(3T)_2PbI_4$, $(4Tm)_2PbI_4$, and $(BTm)_2PbI_4$ thin flakes for in situ high-pressure experiments are shown in fig. S13. The incident laser beam is perpendicular to the diamond culet and parallel to the stacking direction of the 2D layered sample. The pressures were determined by the ruby fluorescence method (*44*). Mineral oil was used as the pressure transmitting medium.

In situ PL and absorption spectroscopy

All the static measurements were performed in a home-designed spectroscopy system in microregion (Gora-UVN-FL, built by Ideaoptics, Shanghai, China). For the absorption measurements, a Xe lamp (EQ-99X-FC-S) was chosen as the white light source. For the PL measurement, a 405-nm continuous laser was used for excitation. The laser beam was focused onto the sample surface by an objective lens (20×, Mitutoyo, 0.42 numerical aperture) with a spot diameter of 3 μm, and the PL emission was collected by the same objective lens. The low-temperature PL spectra were collected on a microscope cryostat system (Janis ST-500). A membrane control system was used to adjust the pressure in situ for the low-temperature PL measurements. The temperature correction of ruby fluorescence is done according to the previous study by Datchi *et al.* (*45*).

In situ TA measurements

For time-resolved femtosecond TA measurements, the fundamental beam produced by the Yb:KGW laser (Pharos, 1030 nm, 20 W, 100 kHz; Light Conversion Ltd.) was separated into several light beams and sent to a homebuilt microscopic ultrafast pump-probe spectrometer collinearly and then lastly combined and focused by a microscope to a spot size of 1 μm. For the pump beam, one of the seed beams was introduced into a commercial noncollinear optical parametric amplifier (2H-NOPA, Light Conversion Ltd.) and a second harmonic generation crystal beta-barium borate (BaB2O4) to generate the pump light with a certain wavelength centered at 470 nm. For the probe beam, another seed beam was focused onto an yttrium-aluminum-garnet crystal (8 mm thickness) to generate continuum white light as the probe light. The temporal delay time between the pump beam and the probe beam was controlled via a high-resolution motorized delay stage (M-ILS250HA, Newport). The pump and probe pulses overlapped spatially at the sample, and the transmitted probe light was collected by a spectrograph (SP2300, Princeton Instruments) coupled to a nitrogen-cooled detector (PyLon100B, Princeton Instruments). The transient transmission signal was calculated by contrasting and normalizing the transmitted probe spectra with and without a pump beam: $\Delta T/T = (T_{pump} - T_{unpump})/T_{unpump}$.

First-principles simulations

First-principles calculations were conducted on the basis of density functional theory through Vienna ab initio simulation package (version 5.4.4) (*46*). The exchange correlation function is approximated by the Perdew-Burke-Ernzerhof (PBE) parametrization revised for solids (*47*, *48*). In this work, the outer shell electrons were modeled by projector-augmented wave function with the following electron configurations: Pb ($5d^{10}6s^26p^2$), I ($5s^25p^5$), S ($3s^23p^4$), C ($2s^22p^2$), N ($2s^22p^3$), and H ($1s^1$); the plane-wave basis set was cut off by a kinetic of 550 eV. We used the PBE-D3 method of Grimme *et al.* (*49*) to correct the long-range atomic interactions. Such computation strategy has successfully reproduced experimental results in a variety of vdW solids (*33*, *50*). The Brillouin zone was sampled at a rate of 0.5 $Å^{-1}$, generating a mesh of 1 × 3 × 2 for all structures, such that the atomic structures were fully optimized until interatomic forces are less than 0.01 eV $Å^{-1}$. We perform geometric relaxation for volume, cell variables, and atomic positions at each target pressure until the force is converged to below the aforementioned threshold. After geometric relaxation, we calculated the energy contribution from spin-orbit coupling to correct the electronic density of states (*51*), as it has shown to qualitatively modify its electronic structure (*36*).

SUPPLEMENTARY MATERIALS

Supplementary material for this article is available at https://science.org/doi/10.1126/sciadv.add1984

REFERENCES AND NOTES

1. X. Xu, Z. Lou, S. Cheng, P. C. Y. Chow, N. Koch, H.-M. Cheng, Van der Waals organic/inorganic heterostructures in the two-dimensional limit. *Chem* **7**, 2989–3026 (2021).

2. A. A. Bakulin, A. Rao, V. G. Pavelyev, P. H. M. van Loosdrecht, M. S. Pshenichnikov, D. Niedzialek, J. Cornil, D. Beljonne, R. H. Friend, The role of driving energy and delocalized states for charge separation in organic semiconductors. *Science* **335**, 1340–1344 (2012).
3. K. S. Novoselov, A. Mishchenko, A. Carvalho, A. H. Castro Neto, 2D materials and van der Waals heterostructures. *Science* **353**, aac9439 (2016).
4. Y. Liu, N. O. Weiss, X. Duan, H.-C. Cheng, Y. Huang, X. Duan, Van der Waals heterostructures and devices. *Nat. Rev. Mater.* **1**, 16042 (2016).
5. N. Wang, L. Cheng, R. Ge, S. Zhang, Y. Miao, W. Zou, C. Yi, Y. Sun, Y. Cao, R. Yang, Y. Wei, Q. Guo, Y. Ke, M. Yu, Y. Jin, Y. Liu, Q. Ding, D. Di, L. Yang, G. Xing, H. Tian, C. Jin, F. Gao, R. H. Friend, J. Wang, W. Huang, Perovskite light-emitting diodes based on solution-processed self-organized multiple quantum wells. *Nat. Photonics* **10**, 699–704 (2016).
6. L. Dou, A. B. Wong, Y. Yu, M. Lai, N. Kornienko, S. W. Eaton, A. Fu, C. G. Bischak, J. Ma, T. Ding, N. S. Ginsberg, L.-W. Wang, A. P. Alivisatos, P. Yang, Atomically thin two-dimensional organic-inorganic hybrid perovskites. *Science* **349**, 1518–1521 (2015).
7. O. P. Dimitriev, Dynamics of excitons in conjugated molecules and organic semiconductor systems. *Chem. Rev.* **122**, 8487–8593 (2022).
8. N. S. Ginsberg, W. A. Tisdale, Spatially resolved photogenerated exciton and charge transport in emerging semiconductors. *Annu. Rev. Phys. Chem.* **71**, 1–30 (2020).
9. E. Shi, Y. Gao, B. P. Finkenauer, Akriti, A. H. Coffey, L. Dou, Two-dimensional halide perovskite nanomaterials and heterostructures. *Chem. Soc. Rev.* **47**, 6046–6072 (2018).
10. B. Zheng, C. Ma, D. Li, J. Lan, Z. Zhang, X. Sun, W. Zheng, T. Yang, C. Zhu, G. Ouyang, G. Xu, X. Zhu, X. Wang, A. Pan, Band alignment engineering in two-dimensional lateral heterostructures. *J. Am. Chem. Soc.* **140**, 11193–11197 (2018).
11. C.-H. Cheng, D. Cordovilla Leon, Z. Li, E. Litvak, P. B. Deotare, Energy transport of hybrid charge-transfer excitons. *ACS Nano* **14**, 10462–10470 (2020).
12. L. Zhao, Y. L. Lin, H. Kim, N. C. Giebink, B. P. Rand, Donor/acceptor charge-transfer states at two-dimensional metal halide perovskite and organic semiconductor interfaces. *ACS Energy Lett.* **3**, 2708–2712 (2018).
13. M. Yuan, L. N. Quan, R. Comin, G. Walters, R. Sabatini, O. Voznyy, S. Hoogland, Y. Zhao, E. M. Beauregard, P. Kanjanaboos, Z. Lu, D. H. Kim, E. H. Sargent, Perovskite energy funnels for efficient light-emitting diodes. *Nat. Nanotechnol.* **11**, 872–877 (2016).
14. E. Shi, B. Yuan, S. B. Shiring, Y. Gao, Akriti, Y. Guo, C. Su, M. Lai, P. Yang, J. Kong, B. M. Savoie, Y. Yu, L. Dou, Two-dimensional halide perovskite lateral epitaxial heterostructures. *Nature* **580**, 614–620 (2020).
15. J. Xue, R. Wang, X. Chen, C. Yao, X. Jin, K.-L. Wang, W. Huang, T. Huang, Y. Zhao, Y. Zhai, D. Meng, S. Tan, R. Liu, Z.-K. Wang, C. Zhu, K. Zhu, M. C. Beard, Y. Yan, Y. Yang, Reconfiguring the band-edge states of photovoltaic perovskites by conjugated organic cations. *Science* **371**, 636–640 (2021).
16. Y. Gao, E. Shi, S. Deng, S. B. Shiring, J. M. Snaider, C. Liang, B. Yuan, R. Song, S. M. Janke, A. Liebman-Pelaez, P. Yoo, M. Zeller, B. W. Boudouris, P. Liao, C. Zhu, V. Blum, Y. Yu, B. M. Savoie, L. Huang, L. Dou, Molecular engineering of organic-inorganic hybrid perovskites quantum wells. *Nat. Chem.* **11**, 1151–1157 (2019).
17. R. Wang, J. Yuan, R. Wang, G. Han, T. Huang, W. Huang, J. Xue, H.-C. Wang, C. Zhang, C. Zhu, P. Cheng, D. Meng, Y. Yi, K.-H. Wei, Y. Zou, Y. Yang, Rational tuning of molecular interaction and energy level alignment enables high-performance organic photovoltaics. *Adv. Mater.* **31**, 1904215 (2019).
18. B. Saparov, D. B. Mitzi, Organic–inorganic perovskites: Structural versatility for functional materials design. *Chem. Rev.* **116**, 4558–4596 (2016).
19. M. T. Greiner, M. G. Helander, W.-M. Tang, Z.-B. Wang, J. Qiu, Z.-H. Lu, Universal energy-level alignment of molecules on metal oxides. *Nat. Mater.* **11**, 76–81 (2012).
20. J. Liu, S. Chen, D. Qian, B. Gautam, G. Yang, J. Zhao, J. Bergqvist, F. Zhang, W. Ma, H. Ade, O. Inganäs, K. Gundogdu, F. Gao, H. Yan, Fast charge separation in a non-fullerene organic solar cell with a small driving force. *Nat. Energy* **1**, 16089 (2016).
21. W. Zheng, B. Zheng, C. Yan, Y. Liu, X. Sun, Z. Qi, T. Yang, Y. Jiang, W. Huang, P. Fan, F. Jiang, W. Ji, X. Wang, A. Pan, Direct vapor growth of 2D vertical heterostructures with tunable band alignments and interfacial charge transfer behaviors. *Adv. Sci.* **6**, 1802204 (2019).
22. A. P. Drozdov, P. P. Kong, V. S. Minkov, S. P. Besedin, M. A. Kuzovnikov, S. Mozaffari, L. Balicas, F. F. Balakirev, D. E. Graf, V. B. Prakapenka, E. Greenberg, D. A. Knyazev, M. Tkacz, M. I. Eremets, Superconductivity at 250 K in lanthanum hydride under high pressures. *Nature* **569**, 528–531 (2019).
23. T. Song, Z. Fei, M. Yankowitz, Z. Lin, Q. Jiang, K. Hwangbo, Q. Zhang, B. Sun, T. Taniguchi, K. Watanabe, M. A. McGuire, D. Graf, T. Cao, J. H. Chu, D. H. Cobden, C. R. Dean, D. Xiao, X. Xu, Switching 2D magnetic states via pressure tuning of layer stacking. *Nat. Mater.* **18**, 1298–1302 (2019).
24. S. Huang, Y. Lu, F. Wang, Y. Lei, C. Song, J. Zhang, Q. Xing, C. Wang, Y. Xie, L. Mu, G. Zhang, H. Yan, B. Chen, H. Yan, Layer-dependent pressure effect on the electronic structure of 2D black phosphorus. *Phys. Rev. Lett.* **127**, 186401 (2021).
25. X. Lü, C. Stoumpos, Q. Hu, X. Ma, D. Zhang, S. Guo, J. Hoffman, K. Bu, X. Guo, Y. Wang, C. Ji, H. Chen, H. Xu, Q. Jia, W. Yang, M. G. Kanatzidis, H.-K. Mao, Regulating off-centering distortion maximizes photoluminescence in halide perovskites. *Natl. Sci. Rev.* **8**, nwaa288 (2021).
26. S. Guo, K. Bu, J. Li, Q. Hu, H. Luo, Y. He, Y. Wu, D. Zhang, Y. Zhao, W. Yang, M. G. Kanatzidis, X. Lu, Enhanced photocurrent of all-inorganic two-dimensional perovskite $Cs_2PbI_2Cl_2$ via pressure-regulated excitonic features. *J. Am. Chem. Soc.* **143**, 2545–2551 (2021).
27. H. Luo, S. Guo, Y. Zhang, K. Bu, H. Lin, Y. Wang, Y. Yin, D. Zhang, S. Jin, W. Zhang, W. Yang, B. Ma, X. Lü, Regulating exciton-phonon coupling to achieve a near-unity photoluminescence quantum yield in one-dimensional hybrid metal halides. *Adv. Sci.* **8**, e2100786 (2021).
28. K. Bu, Q. Hu, X. Qi, D. Wang, S. Guo, H. Luo, T. Lin, X. Guo, Q. Zeng, Y. Ding, F. Huang, W. Yang, H.-K. Mao, X. Lü, Nested order-disorder framework containing a crystalline matrix with self-filled amorphous-like innards. *Nat. Commun.* **13**, 4650 (2022).
29. T. Yin, B. Liu, J. Yan, Y. Fang, M. Chen, W. K. Chong, S. Jiang, J. L. Kuo, J. Fang, P. Liang, S. Wei, K. P. Loh, T. C. Sum, T. J. White, Z. X. Shen, Pressure-engineered structural and optical properties of two-dimensional $(C_4H_9NH_3)_2PbI_4$ perovskite exfoliated nm-thin flakes. *J. Am. Chem. Soc.* **141**, 1235–1241 (2019).
30. S. Liu, S. Sun, C. K. Gan, A. G. del Águila, Y. Fang, J. Xing, T. T. H. Do, T. J. White, H. Li, W. Huang, Q. Xiong, Manipulating efficient light emission in two-dimensional perovskite crystals by pressure-induced anisotropic deformation. *Sci. Adv.* **5**, eaav9445 (2019).
31. R. Fu, W. Zhao, L. Wang, Z. Ma, G. Xiao, B. Zou, Pressure-induced emission toward harvesting cold white light from warm white light. *Angew. Chem. Int. Ed.* **60**, 10082–10088 (2021).
32. S. Guo, Y. Zhao, K. Bu, Y. Fu, H. Luo, M. Chen, M. P. Hautzinger, Y. Wang, S. Jin, W. Yang, X. Lu, Pressure-suppressed carrier trapping leads to enhanced emission in two-dimensional perovskite $(HA)_2(GA)Pb_2I_7$. *Angew. Chem. Int. Ed.* **59**, 17533–17539 (2020).
33. Y. Wang, S. Guo, H. Luo, C. Zhou, H. Lin, X. Ma, Q. Hu, M. H. Du, B. Ma, W. Yang, X. Lu, Reaching 90% photoluminescence quantum yield in one-dimensional metal halide $C_4N_2H_{14}PbBr_4$ by pressure-suppressed nonradiative loss. *J. Am. Chem. Soc.* **142**, 16001–16006 (2020).
34. Z. Ma, Z. Liu, S. Lu, L. Wang, X. Feng, D. Yang, K. Wang, G. Xiao, L. Zhang, S. A. T. Redfern, B. Zou, Pressure-induced emission of cesium lead halide perovskite nanocrystals. *Nat. Commun.* **9**, 4506 (2018).
35. Q. Li, Z. Chen, B. Yang, L. Tan, B. Xu, J. Han, Y. Zhao, J. Tang, Z. Quan, Pressure-induced remarkable enhancement of self-trapped exciton emission in one-dimensional $CsCu_2I_3$ with tetrahedral units. *J. Am. Chem. Soc.* **142**, 1786–1791 (2020).
36. J. J. Yang, W. K. Chen, X. Y. Liu, W. H. Fang, G. Cui, Spin-orbit coupling is the key to promote asynchronous photoinduced charge transfer of two-dimensional perovskites. *JACS Au* **1**, 1178–1186 (2021).
37. J. F. Sierra, J. Fabian, R. K. Kawakami, S. Roche, S. O. Valenzuela, Van der Waals heterostructures for spintronics and opto-spintronics. *Nat. Nanotechnol.* **16**, 856–868 (2021).
38. N. P. Wilson, W. Yao, J. Shan, X. Xu, Excitons and emergent quantum phenomena in stacked 2D semiconductors. *Nature* **599**, 383–392 (2021).
39. L. Pi, P. Wang, S.-J. Liang, P. Luo, H. Wang, D. Li, Z. Li, P. Chen, X. Zhou, F. Miao, T. Zhai, Broadband convolutional processing using band-alignment-tunable heterostructures. *Nat. Electron.* **5**, 248–254 (2022).
40. D. Pan, Y. Fu, N. Spitha, Y. Zhao, C. R. Roy, D. J. Morrow, D. D. Kohler, J. C. Wright, S. Jin, Deterministic fabrication of arbitrary vertical heterostructures of two-dimensional Ruddlesden-Popper halide perovskites. *Nat. Nanotechnol.* **16**, 159–165 (2021).
41. Akriti, E. Shi, S. B. Shiring, J. Yang, C. L. Atencio-Martinez, B. Yuan, X. Hu, Y. Gao, B. P. Finkenauer, A. J. Pistone, Y. Yu, P. Liao, B. M. Savoie, L. Dou, Layer-by-layer anionic diffusion in two-dimensional halide perovskite vertical heterostructures. *Nat. Nanotechnol.* **16**, 584–591 (2021).
42. Y. Fu, W. Zheng, X. Wang, M. P. Hautzinger, D. Pan, L. Dang, J. C. Wright, A. Pan, S. Jin, Multicolor heterostructures of two-dimensional layered halide perovskites that show interlayer energy transfer. *J. Am. Chem. Soc.* **140**, 15675–15683 (2018).
43. J. Xia, J. Yan, Z. Wang, Y. He, Y. Gong, W. Chen, T. C. Sum, Z. Liu, P. M. Ajayan, Z. Shen, Strong coupling and pressure engineering in WSe2–MoSe2 heterobilayers. *Nat. Phys.* **17**, 92–98 (2021).
44. H. K. Mao, J. Xu, P. M. Bell, Calibration of the ruby pressure gauge to 800 kbar under quasi-hydrostatic conditions. *J. Geophys. Res.* **91**, 4673–4676 (1986).
45. F. Datchi, A. Dewaele, P. Loubeyre, R. Letoullec, Y. Le Godec, B. Canny, Optical pressure sensors for high-pressure–high-temperature studies in a diamond anvil cell. *High Pressure Res.* **27**, 447–463 (2007).
46. G. Kresse, J. Hafner, *Ab* initio molecular-dynamics simulation of the liquid-metal–amorphous-semiconductor transition in germanium. *Phys. Rev. B* **49**, 14251–14269 (1994).
47. J. P. Perdew, K. Burke, M. Ernzerhof, Generalized gradient approximation made simple. *Phys. Rev. Lett.* **77**, 3865–3868 (1996).
48. J. P. Perdew, A. Ruzsinszky, G. I. Csonka, O. A. Vydrov, G. E. Scuseria, L. A. Constantin, X. Zhou, K. Burke, Restoring the density-gradient expansion for exchange in solids and surfaces. *Phys. Rev. Lett.* **100**, 136406 (2008).

49. S. Grimme, S. Ehrlich, L. Goerigk, Effect of the damping function in dispersion corrected density functional theory. *J. Compt. Chem.* **32**, 1456–1465 (2011).
50. Z. Cui, K. Bu, Y. Zhuang, M.-E. Donnelly, D. Zhang, P. Dalladay-Simpson, R. T. Howie, J. Zhang, X. Lü, Q. Hu, Phase transition mechanism and bandgap engineering of Sb_2S_3 at gigapascal pressures. *Commun. Chem.* **4**, 125 (2021).
51. S. Steiner, S. Khmelevskyi, M. Marsmann, G. Kresse, Calculation of the magnetic anisotropy with projected-augmented-wave methodology and the case study of disordered $Fe_{1-x}Co_x$ alloys. *Phys. Rev. B* **93**, 224425 (2016).

Acknowledgments
Funding: This work is supported by the National Nature Science Foundation of China (NSFC) (grant no. U1930401). Q.H. is supported by the CAEP Research grant (CX20210048) and the Tencent Xplorer prize (XPLORER-2020-1013). The work by L.D. was supported by the U.S. Department of Energy (DOE), Office of Basic Energy Sciences (BES), under award DE-SC0022082 (perovskite heterostructures). **Author contributions:** S.G., L.D., and X.L. conceived the project. Y.L. and E.S. synthesized single-crystal samples. S.G., Y.M., H.L., and T.F. collected the PL and absorption data. K.B. and Q.H. carried out the first-principles calculations. S.G. and W.T. analyzed the high-pressure TA data with the assistance of C.Z. and H.Z. S.G., X.L., and L.D. wrote the manuscript, revised by Q.H., H.Z., E.S., and W.Y. All authors have interpreted the findings, commented on the paper, and approved the final version. **Competing interests:** The authors declare that they have no competing interests. **Data and materials availability:** All data needed to evaluate the conclusions in the paper are present in the paper and/or the Supplementary Materials.

Submitted 26 May 2022
Accepted 13 September 2022
Published 2 November 2022
10.1126/sciadv.add1984